UC Riverside
UC Riverside Previously Published Works

Title

Mutation-induced shift of the photosystem II active site reveals insight into conserved water channels.

Permalink

https://escholarship.org/uc/item/6df0d9hf

Journal

Journal of Biological Chemistry, 300(7)

Authors

Flesher, David

Liu, Jinchan

Wang, Jimin

et al.

Publication Date

2024-07-01

DOI

10.1016/j.jbc.2024.107475

Peer reviewed

Mutation-induced shift of the photosystem II active site reveals insight into conserved water channels

David A. Flesher[1][iD], Jinchan Liu[1][iD], Jimin Wang[1][iD], Christopher J. Gisriel[2][iD], Ke R. Yang[2][iD], Victor S. Batista[2][iD], Richard J. Debus[3,*][iD], and Gary W. Brudvig[1,2,*][iD]

From the [1]Department of Molecular Biophysics and Biochemistry, Yale University, New Haven, Connecticut, USA; [2]Department of Chemistry, Yale University, New Haven, Connecticut, USA; [3]Department of Biochemistry, University of California, Riverside, California, USA

Reviewed by members of the JBC Editorial Board. Edited by Joseph Jez

Photosystem II (PSII) is the water-plastoquinone photo-oxidoreductase central to oxygenic photosynthesis. PSII has been extensively studied for its ability to catalyze light-driven water oxidation at a Mn_4CaO_5 cluster called the oxygen-evolving complex (OEC). Despite these efforts, the complete reaction mechanism for water oxidation by PSII is still heavily debated. Previous mutagenesis studies have investigated the roles of conserved amino acids, but these studies have lacked a direct structural basis that would allow for a more meaningful interpretation. Here, we report a 2.14-Å resolution cryo-EM structure of a PSII complex containing the substitution Asp170Glu on the D1 subunit. This mutation directly perturbs a bridging carboxylate ligand of the OEC, which alters the spectroscopic properties of the OEC without fully abolishing water oxidation. The structure reveals that the mutation shifts the position of the OEC within the active site without markedly distorting the Mn_4CaO_5 cluster metal-metal geometry, instead shifting the OEC as a rigid body. This shift disturbs the hydrogen-bonding network of structured waters near the OEC, causing disorder in the conserved water channels. This mutation-induced disorder appears consistent with previous FTIR spectroscopic data. We further show using quantum mechanics/molecular mechanics methods that the mutation-induced structural changes can affect the magnetic properties of the OEC by altering the axes of the Jahn-Teller distortion of the Mn(III) ion coordinated to D1-170. These results offer new perspectives on the conserved water channels, the rigid body property of the OEC, and the role of D1-Asp170 in the enzymatic water oxidation mechanism.

Photosystem II (PSII) is the water-splitting enzyme embedded in the thylakoid membrane of green plants, algae, and cyanobacteria (1–3). It fuels photosynthesis by performing light-driven, catalytic water oxidation at the enzyme active site: a Mn_4CaO_5 cluster called the oxygen-evolving complex (OEC,

ref. (4)). The OEC is buried in a highly conserved protein environment and is surrounded by structured water channels that extend to the thylakoid lumen (Fig. 1, refs. (5–7)). While it is understood that the OEC oxidizes water to molecular oxygen in a five-step process, where redox-intermediates are known as S_i states (i = 0–4), many details of the reaction mechanism remain heavily debated, especially the O–O bond formation steps (8, 9). It is only recently that a mechanistic role was identified for a specific pair of conserved carboxylate residues in the Cl-1 water channel (10).

Site-directed mutagenesis on PSII has provided key insights into the water oxidation reaction mechanism, with the vast majority of these studies using the mesophilic cyanobacterium *Synechocystis* sp. PCC 6803 (*Synechocystis* 6803 hereafter, refs. (11–14)). The main reason for this is that *Synechocystis* 6803, unlike most cyanobacteria, can grow photo-heterotrophically on glucose while still expressing PSII (15). This unique characteristic has enabled the study of loss-of-function mutations that probe a perturbed PSII active site. However, accompanying PSII structures from mutated *Synechocystis* 6803 PSII have been unavailable, obscuring the connection between the biophysical data and mutation-induced structural changes. While other high-resolution PSII structures have been available since 2011 (16–18), those structures are all derived from thermophilic cyanobacteria that are obligate, photo-autotrophs that cannot grow with PSII mutations that severely perturb enzyme activity (see Discussion in ref. (19)), including most of the previous mutagenesis studies that specifically target the OEC (11). Furthermore, while the active site is highly conserved between the thermophilic cyanobacteria and *Synechocystis* 6803, sequence and structural differences do exist in the water channels, even as close as 10 Å away from the OEC (5, 20). This makes interpretation of spectroscopic results using the thermophilic cyanobacterial structures potentially problematic, especially since many of these results indicate changes in the hydrogen-bond networks surrounding the OEC (21–27). Therefore, a study that compares the structure and spectroscopy within the same organism is preferable. A recent report resolved several of these complications by providing a high-resolution cryogenic electron microscopy (cryo-EM) structure of wild-type PSII core complexes (WT PSII hereafter) from

* For correspondence: Gary W. Brudvig, gary.brudvig@yale.edu; Richard J. Debus, richard.debus@ucr.edu.
Present address for Ke R. Yang: Key Laboratory of Advanced Energy Materials Chemistry (Ministry of Education), College of Chemistry, Nankai, Tianjin 300071, China.
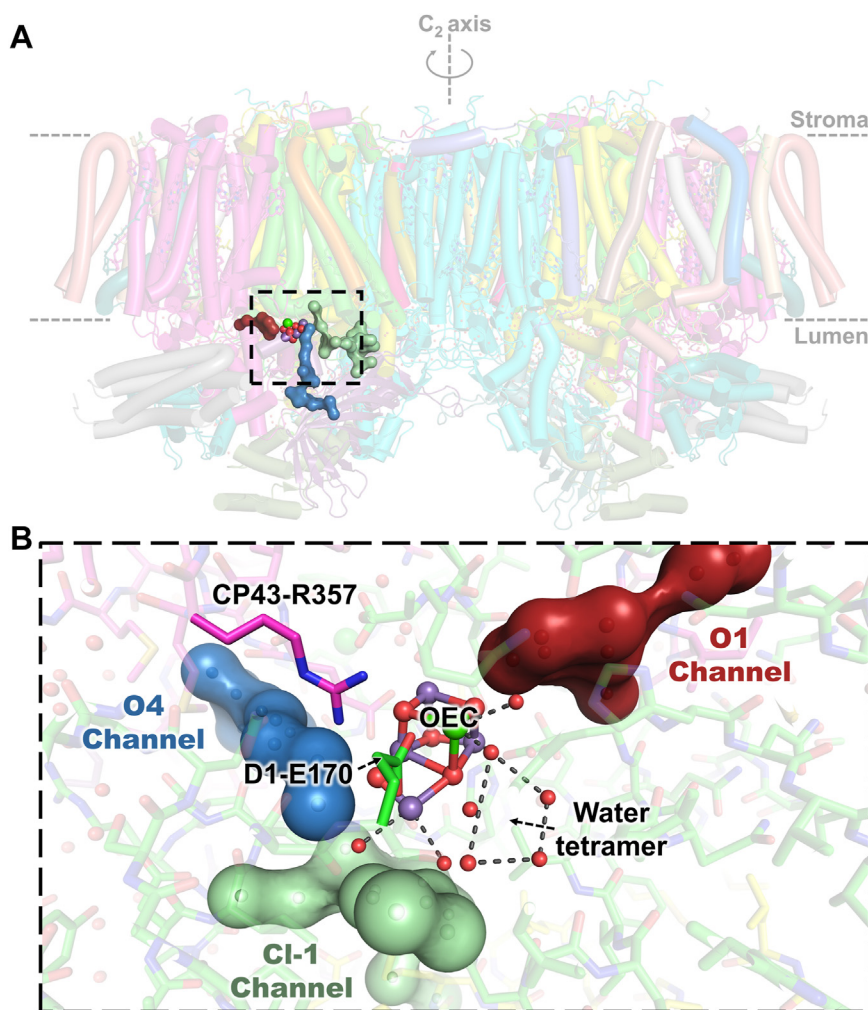
Figure 1. Water channels in photosystem II. *A*, the structure of D1-D170E PSII, colored according to subunit, is shown with portions of the O1 channel, the Cl-1 channel, and the O4 channel shown in *red*, *green*, and *blue* volumes, respectively. *B*, a focused view showing the location of relevant structures in relation to the OEC.

Synechocystis 6803, thus also establishing a platform to investigate the structural basis for many of the site-directed mutations (20).

In the present study, we selected the Asp170Glu mutation on the D1 subunit of PSII for structure-function analysis because it is a relatively conservative Asp to Glu substitution that displays intriguing phenotypes and has been studied with a number of biophysical and spectroscopic techniques. Both cells and isolated PSII core complexes with the D1-D170E mutation evolve O_2 at ∼50% the rate of wild-type (28–32). This is relatively high activity considering that D1-D170 is a bridging ligand to the OEC. Other substitutions to OEC ligands have resulted in a larger decrease of O_2-evolving activity (28, 29). Additionally, recent studies using Fourier transform infrared (FTIR) spectroscopy showed that D1-D170E PSII core complexes (D1-D170E PSII hereafter) have an altered S_2- *minus*$-S_1$ difference spectrum compared to WT PSII, notably in the carboxylate and hydrogen-bonded O–H stretching regions (30). It was hypothesized that the D1-D170E mutation stabilizes an alternate Jahn-Teller distortion of the Mn(III) ion coordinated to D1-170 in the S_1 state, leading to a high-spin

form of the S_2 state (30, 33). A high-spin S_2 state was subsequently identified by electron paramagnetic resonance (EPR) spectroscopy of D1-D170E PSII (34). Previous results for D1-D170E PSII also show reduced O_2 release kinetics and increased miss-factor (35). To investigate the molecular basis for how the water-oxidation mechanism is perturbed by the D1-Asp170Glu substitution, we have solved a 2.14 Å global resolution structure of D1-D170E PSII using cryo-EM and have compared it to the recent WT PSII structure (20).

Results and discussion

Sample preparation and cryo-EM structure

D1-D170E PSII was purified from a mutated strain of *Synechocystis* 6803, as described previously (30). Recent studies have shown that mutations at OEC ligand sites may result in post-translational modification/oxidation, as observed in a His substitution at the D1-170 site (36, 37). To determine whether the D1-D170E mutation was similarly affected, we used liquid chromatography with tandem mass spectrometry to analyze chymotryptic peptides of D1 subunits from purified D1-D170E

and wild-type PSII core complexes. Results indicate that the Asp to Glu mutation is present in D1-D170E PSII and that there has been no post-translational modification/oxidation. This is likely because, unlike the His substitution, the carboxylate group chemistry is conserved. Methods and data are available in the supporting information (Figs. S10 and S11, and Table S7).

Isolated D1-D170E PSII was used for cryo-EM single-particle analysis, yielding a 2.14 Å global resolution map (Figs. S7 and S8, and Table S5). The structure of D1-D170E PSII is dimeric with subunit and cofactor composition nearly identical to WT PSII (Fig. S9, ref. (20)). The OEC has a local resolution of 2.15 Å with highly isotropic map signal amplitude at metal positions but poor signal for oxygen atoms, similar to the WT PSII structure (20, 38). The OEC metal-metal distances for D1-D170E PSII suggest a partially reduced cluster caused by electron radiation damage, as was likewise reported in the WT PSII structure. Further structural details are discussed in the supporting information. Most importantly, the D1-D170E PSII structure reveals the local environment around the OEC at high resolution, allowing for a detailed comparison to the WT PSII structure.

Difference map reveals changes near the OEC

Carefully comparing two cryo-EM structures requires the use of voxel scaling and resolution filtering to minimize the effects of microscope detector differences and mismatched map resolutions between the two structures (39). Without such rescaling, difference map comparisons would create misleading peaks, thus complicating interpretation (39). Using rescaled maps of D1-D170E and WT PSII, we generated a D1-D170E–*minus*–WT difference map to highlight structural changes observed in the mutated PSII structure. The structures were further refined to these rescaled maps and the OEC atoms were placed at the map signal's peak maximum without any restraints (Fig. S3 and Table S6; refs. (9, 20)). The rescaled maps and structures are used throughout the manuscript. This is discussed further in the supporting information.

In D1-D170E PSII, one might expect the longer Glu sidechain to notably displace and distort the OEC relative to the shorter Asp sidechain. However, D1-Glu170 adopts a conformation that "buckles" at the γ-carbon between the OEC and the carbon-backbone (Fig. 2, *A* and *B*), which is in contrast to the other Glu OEC ligands (D1-Glu333, D1-Glu189, and CP43-Glu341) that exhibit a "full-length" conformation (Fig. S6). This somewhat lessens the mutation's effect on the OEC. Nevertheless, the observed D1-Glu170 conformation causes the carboxylate oxygen closest to Ca to notably shift relative to WT PSII (Fig. 1*B*), inducing a translation and rotation of the OEC (animated in Fig. S1). Interestingly, despite this shift, measurements of the OEC metal-metal distances and angles show that the OEC geometry is well maintained relative to WT PSII (Figs. S4 and S5, and Tables S1–S4), indicating that the OEC has behaved as a rigid body rather than distorting in response to the D1-D170E mutation. As a result of the D1-Glu170 conformation and the OEC rigid body
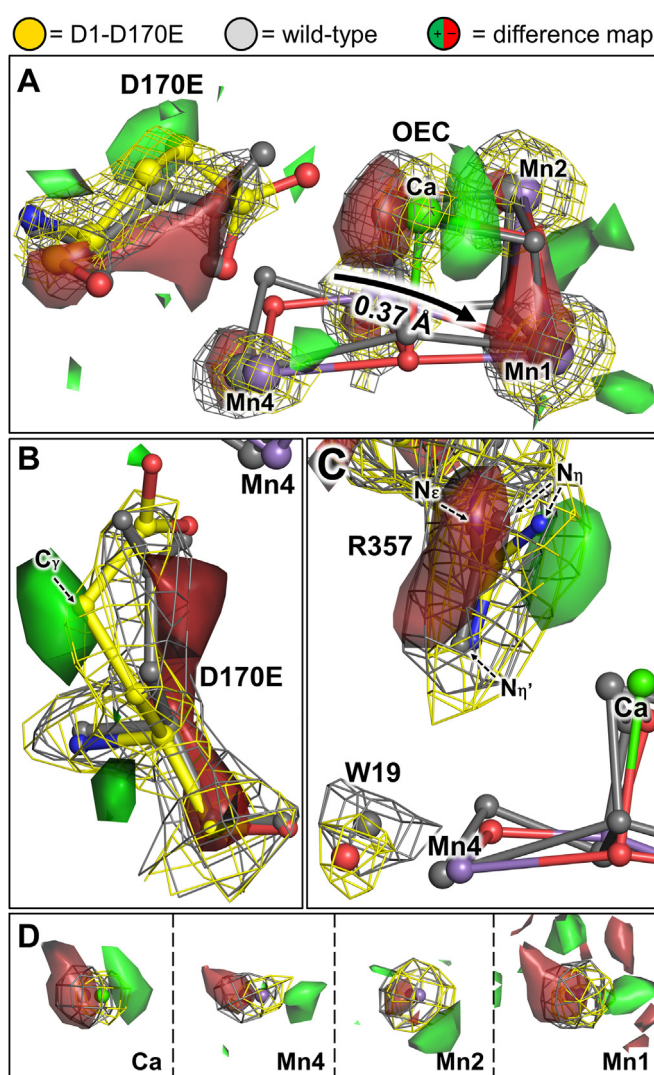

Figure 2. Difference map peaks show changes near the OEC. Overlays of D1-D170E PSII, shown in *yellow*; WT PSII, shown in *grey*; and the D1-D170E-*minus*-WT difference map, shown in positive *green* and negative *red* volumes; (*A*) the Asp to Glu mutation shifting the OEC metal positions, (*B*) the Glu sidechain "buckling," (*C*) CP43-R357 pivoting, and (*D*) individual OEC metals shifting. The rescaled cryo-EM maps and difference maps are shown as isomesh and isosurfaces, respectively. Background map features are excluded for clarity; see Tables S8 and S9 for details.

behavior, the OEC rotates and shifts ~0.37 Å averaged among the OEC metals with Ca experiencing the largest shift of ~0.57 Å due to its proximity to the D1-D170E mutation. These distances are measured between atoms in the rescaled D1-D170E PSII and WT PSII maps; additional measurements for metal and ligand atoms are available in Table S3. This unexpected rigid body behavior may suggest that the OEC is harder to deform than previously thought, possibly supporting OEC models with rigid structures (40, 41). However, it is currently unclear how the OEC oxidation state and electron radiation damage may affect these results.

Arg344 of the CP43 subunit, hereafter referred to by the more common nomenclature CP43-Arg357 based on sequences of PSII from thermophilic cyanobacteria, pivots on the guanidino ε-nitrogen to maintain its salt bridge with the D1-D170E carboxylate group (Fig. 2C). This increases the

distance between the guanidino η'-nitrogen and W19, a structured water in the O4 water channel, weakening that hydrogen-bonding interaction (42). This may contribute to changes observed in the Cl-1 and O4 water channels, as discussed below.

Changes to structured waters

Previous FTIR spectroscopy results suggested that the hydrogen-bonding network near the OEC is significantly perturbed in D1-D170E PSII relative to WT PSII (30), inviting a careful study of water molecules around the OEC between the two structures. However, analyzing water molecules in cryo-EM electrostatic potential (ESP) maps is technically challenging. At very-high resolutions, the signal from highly structured water molecules will appear as spherically symmetric ESP peaks. In contrast, water molecules that have high positional heterogeneity will have non-symmetric ESP peaks, often being elongated in one direction or even becoming completely invisible, a result of peak broadening to levels below detection limits. These misshapen ESP map signals make water placements during modeling highly imprecise and thus the coordinates are unsuitable for detailed analysis. Furthermore, it is currently unclear how electron radiation damage might affect the water signal anisotropy. For our aim, the best method to investigate perturbed waters between the rescaled D1-D170E and WT PSII maps is to analyze the ESP map signal directly, comparing the ESP map signal intensity and degree of anisotropy between the two rescaled maps. This analysis is possible because of the high resolution achieved and because the rescaled maps do not suffer from resolution differences, as described above in the Difference map reveals changes near the OEC section and in the Experimental procedures section.

A comparison of ESP map signals from water molecules surrounding the OEC between the rescaled D1-D170E and WT PSII maps reveals that there are no explicit additions or absences of new water molecules in any of the water channels nearby the OEC, nor any large positional shifts. However, several changes consistent with increased disorder of hydrogen-bonding networks are observed in the Cl-1 water channel, the O4 water channel, and the water tetramer, a four-water structure located between the OEC and D1-Tyr161 (5, 43).

In the O1 water channel, the water channel most distant from the D1-D170E mutation (Fig. 1), water molecule signals and positions appear nearly identically between the rescaled D1-D170E and WT PSII maps (Fig. 3, *D* and *E*). This indicates that the O1 channel is not significantly perturbed in D1-D170E PSII relative to WT PSII and also demonstrates the degree to which conserved water molecules present similar ESP map signals, thus providing a benchmark for other water molecule comparisons.

In the Cl-1 water channel, two waters near the Cl-1 binding site present severely increased ESP map signal anisotropy. This is most noticeable when compared to the same waters in WT PSII and to the nearby Cl-1 ion in D1-D170E PSII, which appears unperturbed relative to WT PSII (Fig. 3*A*). Our interpretation of these changes is an increase in heterogeneity within the Cl-1 channel. This likely results in a decrease in hydrogen-bond directionality, limiting the effectiveness of a Grotthuss-like mechanism for proton egress through the Cl-1 channel, as has recently been demonstrated to occur during the S_3 to S_0 transition (10, 27). This is also consistent with the previously observed decrease in oxygen-release kinetics and increased miss-factor for D1-D170E PSII (35). Similar results were observed in the D2-Lys317Ala mutation, further strengthening the hypothesis that maintaining the conserved hydrogen-bonding network in the Cl-1 channel is crucial for efficient catalytic turnover, especially during O–O bond formation (44).

In the O4 channel, the waters closest to the OEC appear perturbed in the D1-D170E PSII structure relative to WT PSII. The water hydrogen-bonded to CP43-Arg357, W19, appears to shift ∼0.77 Å relative to WT PSII, increasing the distance from CP43-Arg357 and moving towards D1-Asp61 and W1 (Figs. 2*C* and 3*B*). Furthermore, the ESP map signal for waters W48 and W49 appear less spherically symmetric compared to WT PSII. Their relative ESP peak amplitude is also reversed in that W48 has a higher peak amplitude than W49 in D1-D170E PSII, but the opposite is observed in WT PSII (Fig. 3*B*). These observations might result from the shift of W19, thus perturbing the optimal hydrogen-bonding network distances within the O4 channel (45).

In the water tetramer, the geometry of the waters appears altered in D1-D170E PSII relative to WT PSII. In the original WT PSII structure, it was reported that the ESP map suggested alternate water positions for water molecules W3 and W4. Indeed, the WT PSII map is nearly continuous between W3 and the nearby water W24 at very low contours (Fig. 3*C*). In contrast, the D1-D170E PSII map shows a distinctly stabilized alternate water position between W3 and W24 (indicated by an arrow in Fig. 3*C*). This may be associated with the shifted Ca, causing W3, a ligand to Ca, to also shift away, thereby increasing the distance between W3 and W24 and creating space for an alternate water position to be stabilized. While this water molecule is modeled as a new water in D1-D170E PSII, its relatively low signal amplitude indicates it is most likely an alternate position of an existing water molecule. These observations may possibly suggest that, during catalytic turnover, water W3 moves between the water tetramer and W2.

QM/MM calculations deciphering the mechanistic details

In D1-D170E PSII, the altered FTIR and EPR spectra relative to WT PSII were concluded to result from a change in the orientation of the Jahn-Teller distortion of the D1-170 ligated Mn(III) ion in the OEC, which is commonly referred to as Mn4(III) (30, 34). To investigate whether our structural observations are consistent with this conclusion, we have performed quantum mechanics/molecular mechanics (QM/MM) calculations to compare the active site of D1-D170E PSII against WT PSII. We optimized D1-D170E and WT structures in the S_1 state based on the high-oxidation state model of the OEC (46, 47), as described previously (45, 48). These QM/MM

Figure 3. Disorder is observed among structured waters. Water molecules in the (*A*) Cl-1 water channel, (*B*) O4 water channel, (*C*) water tetramer, and (*D* and *E*) O1 water channel are shown for rescaled D1-D170E PSII (*left*), rescaled WT PSII (*middle*), and a merge of rescaled D1-D170E PSII and WT PSII (*right*). *C*, the stabilized water position in the water tetramer is indicated with a *red arrow* in D1-D170E PSII and WT PSII. *D* and *E*, water molecules that are highly conserved between D1-D170E PSII and WT PSII. Throughout, D1-D170E PSII is shown in *yellow* and WT PSII is shown in *grey*. The isomesh shows lower map contour while the isosurface shows a higher map contour. Additional atoms are included for spatial reference but map features are excluded for clarity; see Tables S8 and S9 for details.

optimized structures allow us to examine the OEC with bond distances consistent with the current understanding of the OEC oxidation states (46, 47) rather than using the bond distances observed in the current cryo-EM structures, which are most consistent with an OEC reduced by electron radiation damage (20).

We find that the system is influenced by two distinct and interconvertible hydrogen-bonding networks, that we call

HBN1 and HBN2, which alter the preferred orientation of the Jahn-Teller distortion of the Mn4(III) ion. In HBN1, water W19 donates hydrogen bonds to the OEC O4 oxygen and D1-Asp61 while accepting a hydrogen bond from water W20 (Fig. 4, *A* and *B*). This configuration results in a weaker hydrogen bond between W19 and CP43-Arg357, indicated by the longer bond distance relative to HBN2 (Fig. 4, *A* and *C*). In HBN2, W19 reorients away from D1-Asp61 to instead donate
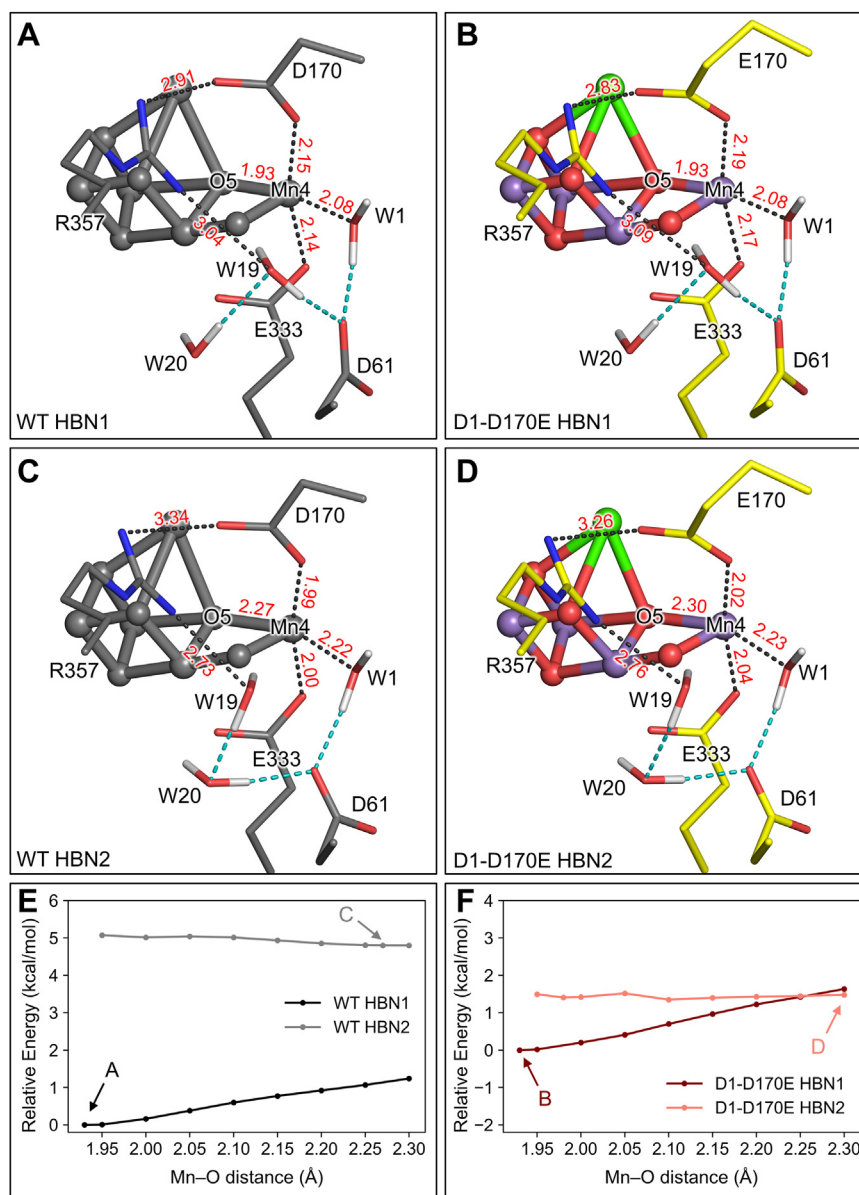
Figure 4. QM/MM calculations show an altered energy landscape for the hydrogen-bonding network (HBN). QM/MM optimized structures for (*A and B*) HBN1 and (*C and D*) HBN2 with labeled distances (Å). *A and C*, show low energy configurations for WT PSII. *B and D*, low-energy configurations for D1-D170E PSII. The relative potential energy landscapes are shown for (*E*) WT PSII and (*F*) D1-D170E PSII configurations, where the energies corresponding to structures in (*A–D*) are annotated.

a hydrogen bond to a reoriented W20, resulting in a much stronger hydrogen bond between W19 and CP43-Arg357, relative to HBN1 (Fig. 4, *A and C*). This change in hydrogen bond strength affects the rest of the system. In HBN1, the weaker hydrogen bond between W19 and CP43-Arg357 results in a stronger salt bridge between CP43-Arg357 and D1-(D/E)170. This weakens the interaction of D1-(D/E)170 and Mn4(III), favoring energetically an elongation of the (D/E)170–Mn4–E333 Jahn-Teller axis (Fig. 4, *A and B*). In contrast, HBN2 has a weaker salt bridge between CP43-Arg357 and D1-(D/E)170 and a stronger interaction between D1-(D/E)170 and Mn4(III), instead favoring energetically an elongation of the W1–Mn4–O5 Jahn-Teller axis (Fig. 4, *C and D*). Therefore, the W19 and W20 hydrogen bond orientation dictates the hydrogen bond strength of CP43-Arg357 and W19, the

strength of the salt bridge between CP43-Arg357 and D1-(D/E)170, the interaction between D1-(D/E)170 and Mn4(III), and the energetically favored Mn4(III) Jahn-Teller elongation axis.

To further study how the two hydrogen-bonding networks alter the equilibrium between the two Jahn-Teller distortions of Mn4(III), we explored the energy landscape along the Mn4–O5 distance, the main reaction coordinate of the Jahn-Teller distortion (Fig. 4, *E and F*). In WT PSII, the calculations show an energy difference of +4.80 kcal/mol between the low energy (D/E)170–Mn4–E333 Jahn-Teller distortion in HBN1 (Fig. 4*A*) and the W1–Mn4–O5 Jahn-Teller distortion in HBN2 (Fig. 4*C*). However, for D1-D170E PSII, the calculations for the same structural configurations show a reduced energy difference of +1.48 kcal/mol (Fig. 4, *B and D*). In both WT PSII and D1-D170E PSII, we find that HBN2 results in a flatter

energy landscape than HBN1. Taken together, the decreased energy difference between HBN1 and HBN2 in D1-D170E and the relatively flat energy landscape of HBN2 suggest that the W1–Mn4–O5 Jahn-Teller distortion has increased abundance in D1-D170E PSII relative to WT PSII. Therefore, these computational results appear consistent with the previous conclusion that D1-D170E PSII has an altered Jahn-Teller distortion of the D1-170 ligated Mn4(III) ion. Furthermore, observations in the cryo-EM maps agree with the QM/MM structures. Both results show a weaker salt bridge between D1-Glu170 and CP43-Arg357 in D1-D170E PSII (Fig. S4 and Table S1). We also observe that the Asp to Glu mutation shifts the carboxylate O1-oxygen atom closer to Mn4(III) in D1-D170E PSII (Fig. S4 and Table S1), disfavoring a Jahn-Teller elongation on the (D/E)170–Mn4–E333 axis in the mutated PSII structure.

Conclusion

We have successfully characterized the D1-D170E PSII cryo-EM structure from *Synechocystis* 6803 to a resolution of 2.14 Å and identified several structural changes relative to WT PSII, thereby providing a molecular basis for previous spectroscopic results. We observe that the D1-Glu170 side chain adopts a "buckled" conformation and causes a mutation-induced shift of the OEC by ∼0.37 Å (Figs. 2A and S1). Interestingly, this does not cause distortion of the OEC geometry relative to WT PSII, indicating that the OEC behaves as a rigid body despite its mutation-induced translation and rotation (Fig. S4 and Tables S1–S4). Similar rigid body behavior might likewise occur in other conservative substitutions of OEC ligands (*e.g.*, D1-D342E, refs. (28, 49)). Overall, D1-D170E PSII maintains the WT OEC ligand interactions, but with altered bond distances (Tables S1–S3). This may explain why D1-D170E PSII has higher oxygen-evolution rates compared to some less conservative mutants that may be more likely to disrupt the OEC ligand environment (12, 28, 29).

In the Cl-1 and O4 water channels, we observe increased positional heterogeneity of waters near the OEC relative to WT PSII, causing disorder in the hydrogen-bonding network (Fig. 3, A–C). This resulted in part from the shifted OEC causing CP43-Arg357 to shift and weaken its interaction with W19 (Fig. 2C). The O1 water channel appears unperturbed (Fig. 3, D and E). Notably, we did not observe any deleted, shifted, or new water molecules in the water channels, other than the previously mentioned W19. This suggests that the observed hydrogen-bonding network disorder is the source of the broad positive and negative features observed in the strongly and weakly hydrogen-bonded O–H stretching regions of the S_2–minus–S_1 FTIR difference spectra of D1-D170E PSII (30). Interestingly, these FTIR features are observed in several mutations (*e.g.*, D1-D61A, D1-S169A, D1-V185N, and D1-N298A; refs. (23–25, 50)), suggesting that these mutants might similarly have mutation-induced disorder in the hydrogen-bonding network, not rearranged water channels. This would further emphasize the importance and delicateness

of conserved features in the hydrogen-bonding network and their mechanistic role in water oxidation.

To investigate the hypothesis that the D1-D170E mutation alters the equilibrium between two Jahn-Teller distortions of the Mn(III) ion coordinated to D1-170, we performed QM/MM calculations of the S_1 state to evaluate the equilibrium energy landscape. Our QM/MM results agree with the cryo-EM observations and highlight how the D1-D170E mutation can affect the magnetic properties of the OEC in ways which are consistent with recent FTIR (30) and EPR spectroscopic (34) results for D1-D170E PSII.

In conclusion, the D1-D170E PSII structure reveals unexpected mutation-induced changes, improving our understanding of previous results and the catalytic mechanism of biological water oxidation. It furthermore demonstrates the feasibility of structurally studying PSII mutants that perturb the OEC, opening the door for future studies.

Experimental procedures

Sample purification

Construction of the D1-D170E mutation of *Synechocystis* sp. PCC 6803 has been described previously (30). The mutation was constructed in the *psbA-2* gene in a host strain that lacks *psbA-1* and *psbA-3* and has a hexahistidine tag fused to the C-terminus of CP47. Isolated PSII core complexes were purified with a Ni-NTA superflow affinity resin (Qiagen, Inc) under minimal green light at 4 °C as described previously (30). The purified samples were concentrated to 1 mg of Chl mL^{-1}, frozen in liquid nitrogen, and stored at –80 °C in the purification buffer (1.2 M betaine, 10% [vol/vol] glycerol, 50 mM MES-NaOH [pH 6.0], 20 mM CaCl$_2$, 5 mM MgCl$_2$, 50 mM histidine, 1 mM EDTA, and 0.03% [wt/vol] n-dodecyl β-D-maltoside [β-DDM]). For cryo-EM analyses, thawed samples were exchanged into cryo-EM buffer (0.5 M betaine, 50 mM MES-NaOH [pH 6.8], 20 mM CaCl$_2$, 5 mM MgCl$_2$, and 0.02% [w/v] β-DDM) at 4 °C by passage through Bio-Rad Micro Bio-Spin 6 centrifugal gel filtration columns (Bio-Rad Laboratories) at 50g. Samples were then concentrated to ∼2 mg of Chl/ml with Amicon Ultra 0.5-mL 100-kDa centrifugal filter devices (EMD Millipore) and kept at ∼4 °C until being loaded onto cryo-EM grids.

Cryo-EM methods

Grid preparation

Holey carbon QUANTIFOIL R 2/1 Cu 300-mesh EM grids (purchased from Electron Microscopy Sciences) were glow discharged for 30 s at 25 mA. Plunge freezing was performed under minimal green light using a FEI Vitrobot (Thermo Fisher Scientific) set to 100% humidity, 4 °C, blot force of 0, and blot time of 3 s. The sample was kept at 4 °C and in complete darkness until 3 µl was quickly applied to the grid under minimal green light. The grid was blotted, plunged into liquid ethane, and stored in liquid nitrogen until data collection. Eight grids were prepared with dilutions in cryo-EM buffer ranging from 0.33 mg of Chl mL^{-1} to 2 mg Chl mL^{-1}.

Structure of the photosystem II D1-D170E mutation

Sample screening and data collection

Sample grids were screened using a Glacios transmission electron microscope (Thermo Fisher Scientific) at low magnification to assess ice thickness and sample distribution. One grid square was examined at high resolution to assess particle homogeneity and this square was excluded from later data collection. Acceptable grids were recovered under liquid nitrogen and sent to the Laboratory for BioMolecular Structure (LBMS) at Brookhaven National Laboratory for data collection on a Titan Krios G2 transmission electron microscope (Thermo Fischer Scientific/FEI) operated at 300 keV with a Gatan K3 direct electron detector in superresolution mode. Data were collected with the following parameters: defocus range of –1.0 to –2 µm, a magnification of 105,000×, a pixel size of 0.825 Å/pix, GIF slit size of 20 eV, a total exposure time of 1.72 s, 56 total frames, and a total dose of 38 e $Å^{-2}$. A total of 8635 micrographs were collected.

Data processing and model building

Cryo-EM single particle analysis was performed using Relion 3.1-beta (51). A complete pipeline with included processing details is shown in Fig. S7. It is worth noting that micelle subtraction, a method commonly used to exclude the detergent micelle from data processing to possibly improve resolution, was attempted but did not yield improved resolution and was therefore omitted. The map resolution was determined using the Gold-standard Fourier Shell Correlation of 0.143. The FSC curve, map local resolution, and angular distribution of particles were calculated by Relion.

Using the sharpened and unsharpened maps generated by Relion, model building was performed using Coot (52) version 0.9.8.1. The WT structure (20) was used as the structural template. Automated refinement was performed in Phenix (53) version 1.19.2-4158 using real_space_refine (54) with NQH flips turned off and nonbonded weight set to 1000. Metal ions, notably those for the OEC, Cl-1, and Cl-2, were placed at peak centroids as described below. The placement of oxygen atoms in the OEC is unreliable and included by convention. Local resolution, angular distribution, and FSC curves are shown in Fig. S8. Analysis confirming C2 symmetry of the ESP map is shown in Fig. S9.

OEC coordinate placement method

In brief, the OEC metal atoms are directly placed at the ESP map peak maxima, that we call the centroid method. This is in contrast to a method using chemical bond restraints that influence the OEC atom positions based on expected bond distances for a given oxidation state model. Placing the metals at the map maxima is also possible because each metal has a strong, spherically symmetric ESP peak, allowing for accurate determination of the atom position. This was done using ChimeraX fitmap commands using the unsharpened map. Further discussion on the rationale and detailed methods for this approach are available as supporting text.

Map voxel/resolution scaling and fitting

Rescaled maps of D1-D170E PSII and WT PSII were used to generate difference maps. These rescaled maps were calculated as described previously (39). In brief, the unsharpened maps of D1-D170E PSII and WT PSII were voxel rescaled to maximize map overlap within ChimeraX (55) using the command fitmap. A ChimeraX script for this is provided in the supplemental GitHub repository. Here, the D1-D170E PSII map is compared to the 7RCV map of WT PSII, as opposed to 7N8O, because it yielded smaller peak amplitude differences (20). The two structures were Fourier-inverted using the program Phenix (56) and then resolution scaled using the scaleit program of the CCP4 package (57). After being rescaled and aligned within ChimeraX, the vector-difference Fourier map for D1-D170E–*minus*–WT was calculated using *fft* in CCP4 (39, 57).

The newly voxel and resolution rescaled D1-D170E PSII and WT PSII maps were then used to re-refine the D1-D170E PSII and WT PSII coordinates, respectively, using Coot, Phenix real-space refine, and the previously mentioned centroid method (52, 54). This is necessary because the model coordinates, particularly those for the transmembrane α-helices, were originally fit to an expanded/shrunken map and the resulting difference adds up across the membrane. Without correcting this, the carbon backbone would be poorly fit, increasing error in sidechain distance measurements. Additional discussion is available as supplementary text. Validation reports for the re-refined models are provided in Table S6.

QM/MM model and computational details

QM/MM calculations were performed to investigate the equilibrium of the isomers with different Jahn-Teller axes in D1-D170E PSII and WT PSII. We built our QM/MM models and optimized structures to reflect the D1-D170E PSII and WT PSII structures from *Synechocystis* 6803 by modifying our previous models built using coordinates by Umena *et al.* (2011, PDB 3WU2, ref. (16)). We identified HBN1 and HBN2 by exploring the different hydrogen bond directions that the water molecules can adopt and noticing that the different hydrogen-bonding configurations produce distinct interactions between CP43-Arg357, D1-(D/E)170, and Mn4(III). When constructing the QM/MM models, the hydrogen bonding directions were manually oriented in the starting states for optimizations and then converged to the different local minima found in HBN1 and HBN2.

The models include residues whose alpha carbon is within 15 Å of the OEC. Acetyl (ACE) and CH_3NH (NME) are used as capping residues for the boundary, with fixed positions during the optimization. We include the OEC; one Cl^- ion; 13 water molecules; the side chains of D1-D61, D1-N181, D1-E189, D1-H332, D1-E333, D1-H337, D1-D342, D1-A344, CP43-E354, CP43-R357, and D2-K317; and the whole residue of D1-S169, D1-(D/E)170, and D1-G171 in the QM layer. The structures were optimized using the ONIOM method (58) in Gaussian16 Rev. C01 ref. (59). The QM layer employed the B3LYP functional (60, 61) with the LanL2DZ pseudopotential and basis set (62, 63) for Mn and Ca, the 6-31G(d) basis set

(64) for O and Cl, the 6-31G for H, C and N. The MM layer was calculated using the AMBER force field (65). QM/MM coordinate files are provided in the supplemental GitHub repository.

Data availability

Cryo-EM data, including rescaled maps for D1-D170E PSII and WT PSII, have been deposited in the Protein Data Bank (https://www.rcsb.org) under accession code 8TOW and the Electron Microscopy Data Bank (https://www.ebi.ac.uk/emdb/) under accession code EMD-41460.

Coordinates for computational models, coordinates for the rescaled D1-D170E PSII and rescaled WT PSII structures, and scripts used for data analysis are available at the GitHub repository https://github.com/DavidAFlesher/D1-D170E_versus_WT_2023.

Conflict of interest—The authors declare that they have no conflicts of interest with the contents of this article.

Abbreviations—The abbreviations used are: cryo-EM, cryogenic electron microscopy; FTIR, Fourier transform infrared; OEC, oxygen-evolving complex; PSII, Photosystem II.

References

1. Blankenship, R. E. (2021) *Molecular Mechanisms of Photosynthesis*, 3rd ed., John Wiley & Sons, Hoboken, NJ

2. Cox, N., Pantazis, D. A., and Lubitz, W. (2020) Current understanding of the mechanism of water oxidation in photosystem II and its relation to XFEL data. *Annu. Rev. Biochem.* **89**, 795–820

3. Shevela, D., Kern, J. F., Govindjee, G., and Messinger, J. (2023) Solar energy conversion by photosystem II: principles and structures. *Photosynth. Res.* **156**, 279–307

4. Vinyard, D. J., and Brudvig, G. W. (2017) Progress toward a molecular mechanism of water oxidation in photosystem II. *Annu. Rev. Phys. Chem.* **68**, 101–116

5. Hussein, R., Ibrahim, M., Bhowmick, A., Simon, P. S., Bogacz, I., Doyle, M. D., *et al.* (2023) Evolutionary diversity of proton and water channels on the oxidizing side of photosystem II and their relevance to function. *Photosynth. Res.* **158**, 91–107

6. Murray, J. W., and Barber, J. (2007) Structural characteristics of channels and pathways in photosystem II including the identification of an oxygen channel. *J. Struct. Biol.* **159**, 228–237

7. Sirohiwal, A., and Pantazis, D. A. (2022) Functional water networks in fully hydrated photosystem II. *J. Am. Chem. Soc.* **144**, 22035–22050

8. Kok, B., Forbush, B., and McGloin, M. (1970) Cooperation of charges in photosynthetic O_2 evolution–I. a linear four step mechanism. *Photochem. Photobiol.* **11**, 457–475

9. Drosou, M., Comas-Vilà, G., Neese, F., Salvador, P., and Pantazis, D. A. (2023) Does serial femtosecond crystallography depict state-specific catalytic intermediates of the oxygen-evolving complex? *J. Am. Chem. Soc.* **145**, 10604–10621

10. Greife, P., Schönborn, M., Capone, M., Assunção, R., Narzi, D., Guidoni, L., *et al.* (2023) The electron–proton bottleneck of photosynthetic oxygen evolution. *Nature* **617**, 623–628

11. Debus, R. J. (2008) Protein ligation of the photosynthetic oxygen-evolving center. *Coord. Chem. Rev.* **252**, 244–258

12. Debus, R. J. (2015) FTIR studies of metal ligands, networks of hydrogen bonds, and water molecules near the active site Mn_4CaO_5 cluster in photosystem II. *Biochim. Biophys. Acta Bioenerg.* **1847**, 19–34

13. Hwang, H. J., Dilbeck, P., Debus, R. J., and Burnap, R. L. (2007) Mutation of Arginine 357 of the CP43 protein of photosystem II severely impairs the catalytic S-state cycle of the H_2O oxidation complex. *Biochemistry* **46**, 11987–11997

14. Dilbeck, P. L., Bao, H., Neveu, C. L., and Burnap, R. L. (2013) Perturbing the water cavity surrounding the manganese cluster by mutating the residue D1-Valine 185 has a strong effect on the water oxidation mechanism of photosystem II. *Biochemistry* **52**, 6824–6833

15. Williams, J. G. K. (1988) Construction of specific mutations in photosystem II photosynthetic reaction center by genetic engineering methods in *Synechocystis* 6803. *Methods Enzymol.* **167**, 766–778

16. Umena, Y., Kawakami, K., Shen, J.-R., and Kamiya, N. (2011) Crystal structure of oxygen-evolving photosystem II at a resolution of 1.9 Å. *Nature* **473**, 55–60

17. Kupitz, C., Basu, S., Grotjohann, I., Fromme, R., Zatsepin, N. A., Rendek, K. N., *et al.* (2014) Serial time-resolved crystallography of photosystem II using a femtosecond X-ray laser. *Nature* **513**, 261–265

18. Kern, J., Tran, R., Alonso-Mori, R., Koroidov, S., Echols, N., Hattne, J., *et al.* (2014) Taking snapshots of photosynthetic water oxidation using femtosecond X-ray diffraction and spectroscopy. *Nat. Commun.* **5**, 4371

19. Sugiura, M., Rappaport, F., Brettel, K., Noguchi, T., Rutherford, A. W., and Boussac, A. (2004) Site-directed mutagenesis of *Thermosynechococcus elongatus* photosystem II: the O_2-evolving enzyme lacking the redox-active Tyrosine D. *Biochemistry* **43**, 13549–13563

20. Gisriel, C. J., Wang, J., Liu, J., Flesher, D. A., Reiss, K. M., Huang, H.-L., *et al.* (2022) High-resolution cryo-electron microscopy structure of photosystem II from the mesophilic cyanobacterium, *Synechocystis* sp. PCC 6803. *Proc. Natl. Acad. Sci. U. S. A.* **119**, e2116765118

21. Service, R. J., Hillier, W., and Debus, R. J. (2014) Network of hydrogen bonds near the oxygen-ovolving Mn_4CaO_5 cluster of photosystem II probed with FTIR difference spectroscopy. *Biochemistry* **53**, 1001–1017

22. Service, R. J., Hillier, W., and Debus, R. J. (2010) Evidence from FTIR difference spectroscopy of an extensive network of hydrogen bonds near

the oxygen-evolving Mn_4Ca cluster of photosystem II Involving D1-Glu65, D2-Glu312, and D1-Glu329. *Biochemistry* **49**, 6655–6669

23. Debus, R. J. (2014) Evidence from FTIR difference spectroscopy that D1-Asp61 influences the water reactions of the oxygen-evolving Mn_4CaO_5 cluster of photosystem II. *Biochemistry* **53**, 2941–2955

24. Nagao, R., Ueoka-Nakanishi, H., and Noguchi, T. (2017) D1-Asn-298 in photosystem II is involved in a hydrogen-bond network near the redox-active tyrosine Y_Z for proton exit during water oxidation. *J. Biol. Chem.* **292**, 20046–20057

25. Ghosh, I., Banerjee, G., Kim, C. J., Reiss, K., Batista, V. S., Debus, R. J., *et al.* (2019) D1-S169A substitution of photosystem II perturbs water oxidation. *Biochemistry* **58**, 1379–1387

26. Kim, C. J., and Debus, R. J. (2020) Roles of D1-Glu189 and D1-Glu329 in O_2 formation by the water-splitting Mn_4Ca cluster in photosystem II. *Biochemistry* **59**, 3902–3917

27. Kuroda, H., Kawashima, K., Ueda, K., Ikeda, T., Saito, K., Ninomiya, R., *et al.* (2021) Proton transfer pathway from the oxygen-evolving complex in photosystem II substantiated by extensive mutagenesis. *Biochim. Biophys. Acta Bioenerg.* **1862**, 148329

28. Chu, H.-A., Nguyen, A. P., and Debus, R. J. (1994) Site-directed photosystem II mutants with perturbed oxygen-evolving properties. 1. Instability or inefficient assembly of the manganese cluster *in vivo*. *Biochemistry* **33**, 6137–6149

29. Chu, H.-A., Nguyen, A. P., and Debus, R. J. (1994) Site-directed photosystem II mutants with perturbed oxygen-evolving properties. 2. Increased binding or photooxidation of manganese in the absence of the extrinsic 33-kDa polypeptide *in vivo*. *Biochemistry* **33**, 6150–6157

30. Debus, R. J. (2021) Alteration of the O_2-producing Mn_4Ca cluster in photosystem II by the mutation of a metal ligand. *Biochemistry* **60**, 3841–3855

31. Nixon, P. J., and Diner, B. A. (1992) Aspartate 170 of the photosystem II reaction center polypeptide D1 is involved in the assembly of the oxygen-evolving manganese cluster. *Biochemistry* **31**, 942–948

32. Boerner, R. J., Nguyen, A. P., Barry, B. A., and Debus, R. J. (1992) Evidence from directed mutagenesis that aspartate 170 of the D1 polypeptide influences the assembly and/or stability of the manganese cluster in the photosynthetic water-splitting complex. *Biochemistry* **31**, 6660–6672

33. Drosou, M., Zahariou, G., and Pantazis, D. A. (2021) Orientational Jahn–Teller isomerism in the dark-stable state of nature's water oxidase. *Angew. Chem. Int. Ed.* **60**, 13493–13499

34. Chakarawet, K., Debus, R. J., and Britt, R. D. (2023) Mutation of a metal ligand stabilizes the high-spin form of the S_2 state in the O_2-producing Mn_4CaO_5 cluster of photosystem II. *Photosynth. Res.* **156**, 309–314

35. Hwang, H. J., McLain, A., Debus, R. J., and Burnap, R. L. (2007) Photoassembly of the manganese cluster in mutants perturbed in the high affinity Mn-binding site of the H_2O-oxidation complex of photosystem II. *Biochemistry* **46**, 13648–13657

36. Shimada, Y., Suzuki, T., Matsubara, T., Kitajima-Ihara, T., Nagao, R., Dohmae, N., *et al.* (2022) Post-translational amino acid conversion in photosystem II as a possible origin of photosynthetic oxygen evolution. *Nat. Commun.* **13**, 4211

37. Kitajima-Ihara, T., Suzuki, T., Nakamura, S., Shimada, Y., Nagao, R., Dohmae, N., *et al.* (2020) Fourier transform infrared and mass spectrometry analyses of a site-directed mutant of D1-Asp170 as a ligand to the water-oxidizing Mn_4CaO_5 cluster in photosystem II. *Biochim. Biophys. Acta Bioenerg.* **1861**, 148086

38. Askerka, M., Vinyard, D. J., Wang, J., Brudvig, G. W., and Batista, V. S. (2015) Analysis of the radiation-damage-free X-ray structure of photosystem II in light of EXAFS and QM/MM Data. *Biochemistry* **54**, 1713–1716

39. Wang, J., Liu, J., Gisriel, C. J., Wu, S., Maschietto, F., Flesher, D. A., *et al.* (2022) How to correct relative voxel scale factors for calculations of vector-difference Fourier maps in cryo-EM. *J. Struct. Biol.* **214**, 107902

40. Corry, T. A., and O'Malley, P. J. (2019) Proton isomers rationalize the high- and low-spin forms of the S_2 state intermediate in the water-oxidizing reaction of photosystem II. *J. Phys. Chem. Lett.* **10**, 5226–5230

41. Corry, T. A., and O'Malley, P. J. (2020) Molecular identification of a high-spin deprotonated intermediate during the S_2 to S_3 transition of nature's water-oxidizing complex. *J. Am. Chem. Soc.* **142**, 10240–10243

42. Shimada, Y., Suzuki, H., Tsuchiya, T., Mimuro, M., and Noguchi, T. (2011) Structural coupling of an arginine side chain with the oxygen-evolving Mn_4Ca cluster in photosystem II as revealed by isotope-edited Fourier transform infrared spectroscopy. *J. Am. Chem. Soc.* **133**, 3808–3811

43. Kalendra, V., Reiss, K. M., Banerjee, G., Ghosh, I., Baldansuren, A., Batista, V. W. S., *et al.* (2022) Binding of the substrate analog methanol in the oxygen-evolving complex of photosystem II in the D1-N87A genetic variant of cyanobacteria. *Faraday Discuss* **234**, 195–213

44. Pokhrel, R., Service, R. J., Debus, R. J., and Brudvig, G. W. (2013) Mutation of Lysine 317 in the D2 subunit of photosystem II alters chloride binding and proton transport. *Biochemistry* **52**, 4758–4773

45. Flesher, D. A., Liu, J., Wiwczar, J. M., Reiss, K., Yang, K. R., Wang, J., *et al.* (2022) Glycerol binding at the narrow channel of photosystem II stabilizes the low-spin S_2 state of the oxygen-evolving complex. *Photosynth. Res.* **152**, 167–175

46. Krewald, V., Neese, F., and Pantazis, D. A. (2015) Resolving the manganese oxidation states in the oxygen-evolving catalyst of natural photosynthesis. *Isr. J. Chem.* **55**, 1219–1232

47. Chrysina, M., Drosou, M., Castillo, R. G., Reus, M., Neese, F., Krewald, V., *et al.* (2023) Nature of S-states in the oxygen-evolving complex resolved by high-energy resolution fluorescence detected X-ray absorption spectroscopy. *J. Am. Chem. Soc.* **145**, 25579–25594

48. Askerka, M., Wang, J., Brudvig, G. W., and Batista, V. S. (2014) Structural changes in the oxygen-evolving complex of photosystem II induced by the S_1 to S_2 transition: a combined XRD and QM/MM study. *Biochemistry* **53**, 6860–6862

49. Debus, R. J., and Oyala, P. H. (2024) Independent mutation of two bridging carboxylate ligands stabilizes alternate conformers of the photosynthetic O_2-evolving Mn_4CaO_5 cluster in photosystem II. *J. Phys. Chem. B.* **128**, 3870–3884

50. Kim, C. J., Bao, H., Burnap, R. L., and Debus, R. J. (2018) Impact of D1-V185 on the water molecules that facilitate O_2 formation by the catalytic Mn_4CaO_5 cluster in photosystem II. *Biochemistry* **57**, 4299–4311

51. Zivanov, J., Nakane, T., Forsberg, B. O., Kimanius, D., Hagen, W. J., Lindahl, E., *et al.* (2018) New tools for automated high-resolution cryo-EM structure determination in RELION-3. *Elife* **7**, e42166

52. Emsley, P., Lohkamp, B., Scott, W. G., and Cowtan, K. (2010) Features and development of Coot. *Acta Crystallogr. D Biol.* **66**, 486–501

53. Afonine, P. V., Grosse-Kunstleve, R. W., Echols, N., Headd, J. J., Moriarty, N. W., Mustyakimov, M., *et al.* (2012) Towards automated crystallographic structure refinement with phenix.refine. *Acta Crystallogr. D Biol. Crystallogr.* **68**, 352–367

54. Afonine, P. V., Poon, B. K., Read, R. J., Sobolev, O. V., Terwilliger, T. C., Urzhumtsev, A., *et al.* (2018) Real-space refinement in PHENIX for cryo-EM and crystallography. *Acta Crystallogr. D* **74**, 531–544

55. Pettersen, E. F., Goddard, T. D., Huang, C. C., Meng, E. C., Couch, G. S., Croll, T. I., *et al.* (2021) UCSF ChimeraX: structure visualization for researchers, educators, and developers. *Protein Sci.* **30**, 70–82

56. Adams, P. D., Afonine, P. V., Bunkóczi, G., Chen, V. B., Davis, I. W., Echols, N., *et al.* (2010) PHENIX: a comprehensive Python-based system for macromolecular structure solution. *Acta Crystallogr. D Biol. Crystallogr.* **66**, 213–221

57. Winn, M. D., Ballard, C. C., Cowtan, K. D., Dodson, E. J., Emsley, P., Evans, P. R., *et al.* (2011) Overview of the CCP4 suite and current developments. *Acta Crystallogr. D Biol. Crystallogr.* **67**, 235–242

58. Vreven, T., and Morokuma, K. (2000) The ONIOM (our own N-layered integrated molecular orbital + molecular mechanics) method for the first singlet excited (S1) state photoisomerization path of a retinal protonated Schiff base. *J. Chem. Phys.* **113**, 2969–2975

59. Frisch, M. J., Trucks, G. W., Schlegel, H. B., Scuseria, G. E., Robb, M. A., Cheeseman, J. R., *et al.* (2016) *Gaussian 16 Rev. C.01.* Gaussian, Inc, Wallingford, CT

60. Becke, A. D. (1988) Density-functional exchange-energy approximation with correct asymptotic behavior. *Phys. Rev. A.* **38**, 3098–3100

ASBMB

61. Stephens, P. J., Devlin, F. J., Chabalowski, C. F., and Frisch, M. J. (1994) *Ab initio* calculation of vibrational absorption and circular dichroism spectra using density functional force fields. *J. Phys. Chem.* **98**, 11623–11627

62. Hay, P. J., and Wadt, W. R. (1985) Ab initio effective core potentials for molecular calculations. Potentials for K to Au including the outermost core orbitals. *J. Chem. Phys.* **82**, 299–310

63. da Silva Filho, D. A., Coropceanu, V., Fichou, D., Gruhn, N. E., Bill, T. G., Gierschner, J., *et al.* (2007) Hole-vibronic coupling in oligothiophenes: impact of backbone torsional flexibility on relaxation energies. *Phil. Trans. R. Soc. A.* **365**, 1435–1452

64. Hariharan, P. C., and Pople, J. A. (1973) The influence of polarization functions on molecular orbital hydrogenation energies. *Theoret. Chim. Acta* **28**, 213–222

65. Case, D. A., Aktulga, H. M., Belfon, K., Ben-Shalom, I. Y., Brozell, S. R., Cerutti, D. S., *et al.* (2021) *Amber 2021.* University of California, San Francisco, CA

66. Kato, K., Miyazaki, N., Hamaguchi, T., Nakajima, Y., Akita, F., Yonekura, K., *et al.* (2021) High-resolution cryo-EM structure of photosystem II reveals damage from high-dose electron beams. *Commun. Biol.* **4**, 1–11

67. Sigworth, F. J. (2016) Principles of cryo-EM single-particle image processing. *Microscopy* **65**, 57–67

68. Wilkinson, M. E., Kumar, A., and Casañal, A. (2019) Methods for merging data sets in electron cryo-microscopy. *Acta Crystallogr. D Struct. Biol.* **75**, 782–791

69. Wang, J., and Moore, P. B. (2017) On the interpretation of electron microscopic maps of biological macromolecules. *Protein Sci.* **26**, 122–129

70. Bhowmick, A., Hussein, R., Bogacz, I., Simon, P. S., Ibrahim, M., Chatterjee, R., *et al.* (2023) Structural evidence for intermediates during O_2 formation in photosystem II. *Nature* **617**, 629–636

71. Chen, S., McMullan, G., Faruqi, A. R., Murshudov, G. N., Short, J. M., Scheres, S. H. W., *et al.* (2013) High-resolution noise substitution to measure overfitting and validate resolution in 3D structure determination by single particle electron cryomicroscopy. *Ultramicroscopy* **135**, 24–35

72. Rosenthal, P. B., and Henderson, R. (2003) Optimal determination of particle orientation, absolute hand, and contrast loss in single-particle electron cryomicroscopy. *J. Mol. Bio.* **333**, 721–745

73. Woińska, M., Grabowsky, S., Dominiak, P. M., Woźniak, K., and Jayatilaka, D. (2016) Hydrogen atoms can be located accurately and precisely by x-ray crystallography. *Sci. Adv.* **2**, e1600192

74. Cruickshank, D. W. J. (1956) The determination of the anisotropic thermal motion of atoms in crystals. *Acta Cryst.* **9**, 747–753

75. Schrödinger, LLC (2015) *The PyMOL Molecular Graphics System, Version 2.5.1.* Schrödinger, Inc, New York, NY

76. Kern, J., Chatterjee, R., Young, I. D., Fuller, F. D., Lassalle, L., Ibrahim, M., *et al.* (2018) Structures of the intermediates of Kok's photosynthetic water oxidation clock. *Nature* **563**, 421–425

77. Li, H., Nakajima, Y., Nango, E., Owada, S., Yamada, D., Hashimoto, K., *et al.* (2024) Oxygen-evolving photosystem II structures during S_1–S_2–S_3 transitions. *Nature* **626**, 670–677

78. Tanaka, A., Fukushima, Y., and Kamiya, N. (2017) Two different structures of the oxygen-evolving complex in the same polypeptide frameworks of photosystem II. *J. Am. Chem. Soc.* **139**, 1718–1721